

3D morphometry of the human optic nerve head[☆]

Ian A. Sigal^{a,b,*}, John G. Flanagan^{c,d}, Inka Tertinegg^c, C. Ross Ethier^{a,b,c,e}

^a Department of Mechanical & Industrial Engineering, University of Toronto, Toronto, ON, Canada

^b Institute for Biomaterials and Biomedical Engineering, University of Toronto, Toronto, ON, Canada

^c Department of Ophthalmology and Vision Sciences, University of Toronto, Toronto, ON, Canada

^d School of Optometry, University of Waterloo, Waterloo, Canada

^e Department of Bioengineering, Imperial College London, London, United Kingdom

ARTICLE INFO

Article history:

Received 24 February 2009

Accepted in revised form

14 September 2009

Available online 20 September 2009

Keywords:

glaucoma
optic nerve head
morphology
morphometry
lamina cribrosa
pia mater

ABSTRACT

Human optic nerve head (ONH) anatomy is of interest in glaucoma. Our goal was to carry out a morphometric study of the human ONH based on 3D reconstructions from histologic sections. A set of 10 human ONHs (from four pairs of eyes plus two singles) were reconstructed in an iterative procedure that required the resulting geometries to satisfy a set of quality control criteria. Five models corresponded to eyes fixed at 5 mmHg and the other five models to eyes fixed at 50 mmHg. Several aspects of ONH morphology were measured based on surface and point landmarks: the thicknesses of the lamina cribrosa (LC), the peripapillary sclera and the pre-laminar neural tissue (peripapillary and within the cup); the minimum distance between the anterior surface of the LC and the subarachnoid space; the surface area of the anterior and posterior surfaces of the LC; and the diameter of the scleral canal opening. Our results showed that about one third of the anterior LC surface was obscured from view from the front by the sclera. In all eyes the LC inserted into the pia mater, and not only into the sclera. The variations in ONH morphology between eyes of a pair exceeded, or were of the same order as, changes in morphology due to acute changes in IOP. The reconstruction and morphometry techniques introduced are suitable for application to the ONH. Comparison of measurements in eyes fixed at different pressures suggested small effects on geometry of the increase in IOP. A large variability in ONH morphology, even between contralateral eyes of different IOP, was observed. We conclude that reconstruction of human ONH anatomy from 3D histology is possible, but that large inter-individual anatomic variations make morphometric analysis of the ONH very difficult in the absence of large sample numbers. The insertion of the pia mater into the LC may have biomechanical implications and should be further investigated. Emerging clinical imaging techniques such as deep-scanning OCT will be limited to investigation of the central and mid-peripheral regions of the LC due to optical "occluding" by the peripapillary sclera.

© 2009 Elsevier Ltd. All rights reserved.

1. Introduction

The causes of retinal ganglion cell dysfunction - and eventual retinal ganglion cell loss - in glaucomatous optic neuropathy are poorly understood, but likely involve some combination of biomechanical and ischemic factors acting on optic nerve head (ONH) tissues (Burgoyne et al., 2005). Previous work has sought to identify links between anatomic features of the ONH and an

individual's susceptibility to the development and progression of glaucomatous optic neuropathy (Burgoyne et al., 2005; Downs et al., 2007; Jonas et al., 2003, 2004; Quigley et al., 1981).

Characterization of ONH geometry is complicated because of the difficulty of accessing ONH tissues directly. Some researchers have therefore measured ONH surface morphology, searching for correlations between surface features, such as cup depth or volume, and the risk of glaucomatous neuropathy (Jonas and Budde, 2000; Wells et al., 2008). Although these studies are valuable, they have limitations. Specifically, recent work suggests that the ONH surface is probably not a good surrogate for IOP-induced deformations of the interior (Agoumi et al., 2009; Sigal et al., 2004, 2009a; Williams et al., 2009), and that IOP-related ONH biomechanics depend more strongly on the morphology of the ONH interior than on that of the ONH surface (Sigal, 2009; Sigal et al., 2005a, 2004). These limitations can be overcome by using histological samples, as has been

[☆] Supported by Consejo Nacional de Ciencia y Tecnología de México (CONACYT; IAS), Canadian Institutes of Health Research (CRE, JGF); The Glaucoma Research Society of Canada (JGF) and the Canada Research Chairs Program (CRE).

* Correspondence to: Ian A. Sigal, Ocular Biomechanics Laboratory, Devers Eye Institute, 1225 NE 2nd Avenue, Portland, Oregon 97232, USA. Tel.: +1 503 413 5408; fax: +1 503 413 5179.

E-mail address: ian.sigal@gmail.com (I.A. Sigal).

done from monkeys (Burgoyne and Morrison, 2001; Burgoyne et al., 1994; Downs et al., 2007; Yang et al., in press, 2007b), dogs (Morgan, 1999), tree shrews (Albon et al., 2007) and human donors (Jonas et al., 2003, 2004; Oyama et al., 2006; Quigley and Addicks, 1981; Yan et al., 1998). Histological tissue samples can be stained to show tissue composition and imaged with high spatial resolution. However, many of these studies have also been limited since measurements taken from 2D histologic sections are susceptible to artifacts, e.g. related to the angle and location of the section. Recent histomorphometric analysis of the monkey ONH has shown that more robust measurements can be obtained through 3D analysis (Downs et al., 2007; Yang et al., 2007a).

The goal of this manuscript was to demonstrate a method to study human ONH morphology in 3D. In addition to traditional measures of ONH morphology, such as lamina cribrosa (LC) and sclera thickness, this approach enables us to obtain novel measures, such as the area of the LC insertion into the surrounding load-bearing tissues (which is important in the transfer of IOP-induced loads to the LC (Sigal, 2009; Sigal et al., 2005a, 2009a)), and the area of the LC visible through the scleral canal opening (which is important in the interpretation of images of the ONH obtained with deep-scanning OCT).

2. Methods

2.1. Building 3D reconstructions of the ONH

For the present study, ten eyes from six human donors were used (Table 1). Eyes were obtained and managed in accordance with the provisions of the Declaration of Helsinki for research involving human tissue. When a pair of eyes was available, one eye was randomly chosen to be fixed and reconstructed at 5 mmHg, whereas the contralateral eye was processed at 50 mmHg. A full description of the histologic techniques has been presented elsewhere (Sigal et al., 2005b). Briefly, after imaging (which typically took 2.5 h per eye, 3 h per pair), the eyes were fixed using 2.5% paraformaldehyde/2.5% glutaraldehyde in Sorensen's phosphate buffer and the ONH and peripapillary sclera were dissected free from the eye, dehydrated and embedded in JB-4 plastic using a special mould that allowed the placement of tensioned collagen sutures for use as fiducial markers. Serial sagittal sections (2 μ m thick at 100 μ m spacings across the ONH) were cut at right angles to the axes of the fiducial markers and digitally photographed under dark-field illumination (2048 \times 1536 pixels, 8 RGB bits per channel per pixel) ensuring uniform sample illumination and non-saturation of the brightest image regions (typically the sclera). Sections were then stained with picrisirius red to identify collagen and solochrome cyanin to identify myelin, nuclei and blood cells. The dual-stained sections were digitally photographed under bright field illumination using the same procedure.

Images were aligned and unwarped to correct the deformations that occurred during the sectioning process (Fig. 1, top row). This was carried out using a custom modified version of TPSSuper (F. James Rohlf, SUNY, Stony Brook, NY), and was based on the

known fiducial marker positions as cast into the histologic block during the embedding procedure. This method avoided the use of anatomical features for alignment, which can lead to artefacts (Hecksher-Sorensen and Sharpe, 2001). The final magnification of images was determined by using measurements of inter-fiducial distances taken prior to sectioning.

The digital sections were manually segmented to define five tissue regions: sclera, LC, pre-laminar neural tissue (including retina), post-laminar neural tissue (including the optic nerve) and pia mater (Fig. 1, middle row). We used both the dark-field and dual-stained images to different extents depending on the tissue being identified. The concurrent use of both dark and bright field images for the same section improved the decisions taken during reconstruction, since not all features of the geometry were equally visible in all imaging modalities. The sclera was dense and fibrous in the dark-field images, and in the stained images it had the most intense picrisirius staining. The pia mater also stained well for collagen and was bright and amorphous in the dark-field images. The anterior boundary of the LC was defined by the termination of the laminar beams and the insertion points at the sclera, whereas the posterior boundary was defined by two features: the termination of solochrome cyanin staining, indicating a lack of myelination inside the LC (Hernandez, 2000), and the "stacked plate" morphology of the connective tissues typical of the LC (Jonas and Budde, 2000; Quigley and Addicks, 1981). The vitreo-retinal interface was clearly distinguishable in the double-stained images, as were the boundaries where the ONH had been cut from the rest of the eye. To ensure consistency across all eyes, all the segmentations were checked and adjusted by a single observer (JGF).

To generate smooth and anatomically accurate 3D reconstructions it was useful to enrich the image stack by adding virtual sections between the ones obtained from the histology. The new sections were cubic interpolations inserted evenly (\sim 33 μ m apart, i.e. two interpolated sections between a pair of original sections). The interpolated sections were then cleaned of artefacts of interpolation and smoothed in all three projections. Although interpolation did not add any new information, it simplified the production of 3D geometries while preserving a physiologically reasonable morphology.

2.2. Segmentation quality control

Segmentation and 3D reconstruction produced good draft models, but a crucial element of our reconstruction process was its iterative nature. Small iterative refinements were made to the image alignment (translation and rotation), and the segmentation to reduce irregularities. At each step of the iterative process the segmentation could be seen in the same planes as the original and interpolated sections, or in any other plane. To be included in this work, the reconstructed models had to satisfy the following six quality criteria:

1. All tissue interfaces had to be anatomically plausible, e.g. the pre and post-laminar neural tissue regions could not touch.
2. Each region (tissues and exterior) had to be topologically connected in a single volume, i.e. no "islands" or "bubbles".
3. Tissue surfaces had to be smooth, with no bumps, ripples or waves, due for example to the discrete nature of the serial sections.
4. Tissue labelling in the model had to match tissue labelling in the histologic sections. If small adjustments were required during the iterative process to satisfy quality requirements, changes in the segmentation were only accepted if they matched the histologic images. This meant that changes were made mostly to the interpolated sections, leaving the original sections unchanged.

Table 1
Summary of donor information and fixation pressure.

Donor	1	1	2	3	4	4	5	5	6	6
Eye	OD	OS	OD	OD	OD	OS	OD	OS	OD	OS
Age [Years]	83		79	91	76		84		70	
Gender	M		M	M	M		M		M	
Time to enucleation [Hrs]	2		2	10	3		7		7	
Time to imaging [Hrs]	17		23.5	29	19		24		16	
Axial length [mm]	24.5	24.5	23.2	24.4	23.7	23.8	24.7	25.0	24.0	24.0
Fixation pressure [mmHg]	50	5	5	50	5	50	5	50	5	50

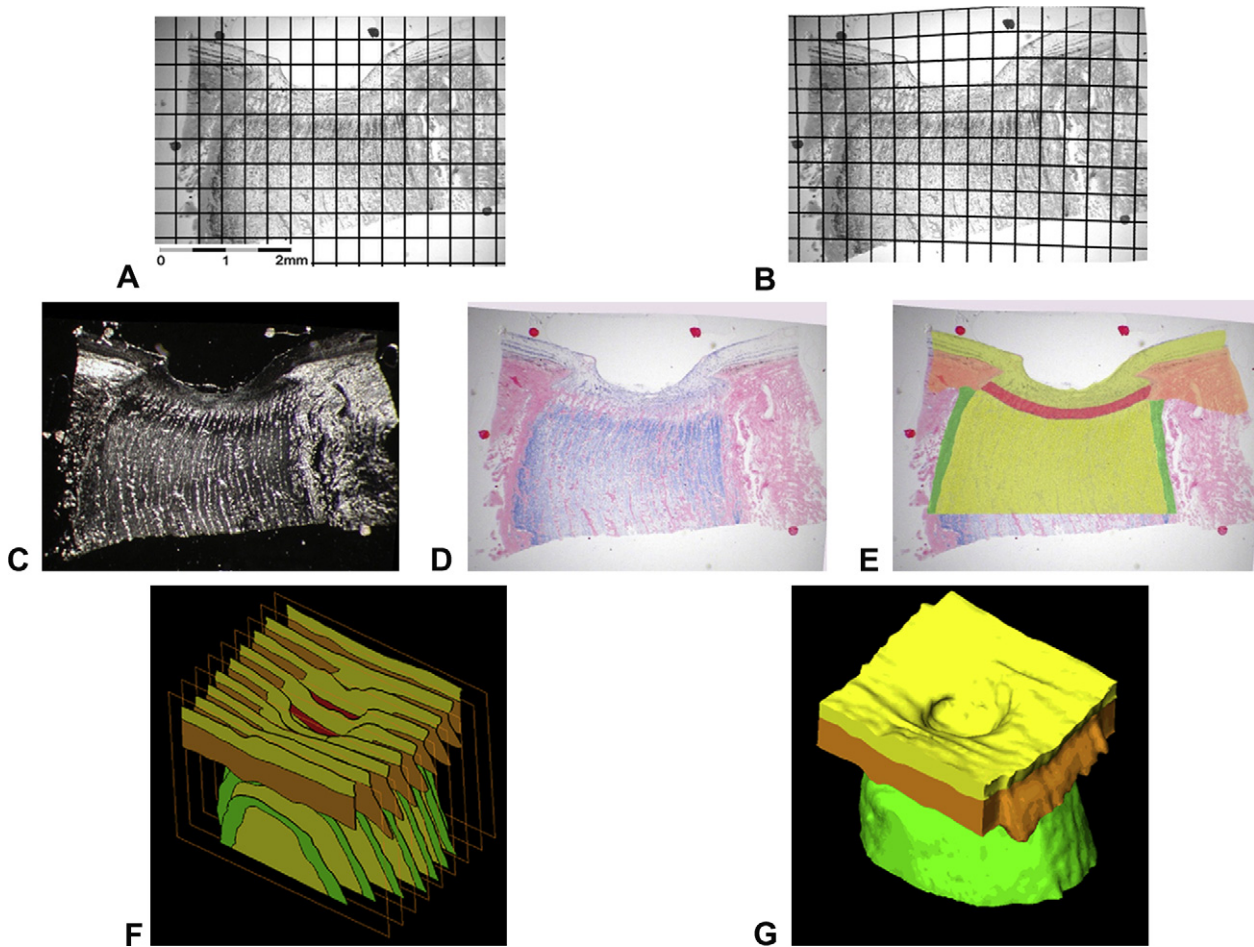


Fig. 1. The process of segmentation and geometry reconstruction. Digital photographs of tissue sections are aligned to form a stack, using fiducial markers inserted before embedding and sectioning (top row). Panel A shows a typical sagittal cross section with superposed square grid. The fiducial markers are the four dark dots. Panel B shows the same section after unwarping for alignment using non-rigid registration. Although the digital photographs were manipulated in color, here we have shown them in greyscale to emphasize the overlaid grid. Segmentation (middle row) used a combination of dark (Panel C) and bright field (Panel D) images of dual-stained sections. The sections were manually segmented to define the tissue regions. During the iterative process of model reconstruction and evaluation the segmentation can be displayed superposed on the histology to check that the reconstructed model is consistent with the histology (Panel E). A stack of sections was then used to reconstruct the 3D geometry of the specimen (Panels F and G). Note that for clarity only a subset of the sections are shown in Panel F. The actual reconstruction was made with between 60 and 90 sections. Five tissues were identified: pre and post-laminar neural tissues (yellow), sclera (orange), lamina cribrosa (red) and pia mater (green). (For interpretation of the references to colour in this figure legend, the reader is referred to the web version of this article.)

5. The pia mater had to be continuous, with no openings through which the post-laminar neural tissue was exposed, except at the surface that represented the cut through the posterior optic nerve. Volume meshing suitable for finite element modeling required a minimum pial thickness of not less than about 70 μm . Thus, when thinner than 70 μm , the pia mater was adjusted by extending the segmentation into the post-laminar neural tissue region. See (Sigal et al., 2009b) for an extended discussion of the effects of pia mater thickness.
6. There should be no sharp edges, as they introduce possible sources of error during numerical modeling. Segmentations were smoothed using a volume-preserving algorithm which adjusted the surfaces less than 5 μm (usually between 1 and 2 μm).

After successful reconstruction, a model consisted of the surfaces delimiting the segmented tissues. Each surface was formed by a collection of triangular elements, each element being defined by three nodes and the inter-nodal connectivity.

The size of the ONH tissue on histologic sections and the length of the optic nerve varied from eye to eye. To fairly compare volumes between eyes, a region of interest (ROI) was defined based on the

area of the anterior surface of the LC, following the methodology described in (Sigal et al., 2007a). Only tissues within the ROI were considered for the calculations of volumes and the analysis of distributions (means and percentiles).

2.3. Morphometry

All morphometry was performed in a masked fashion, i.e. using coded files that had been stripped of all information that would identify the eye number or level of IOP at which the eye was fixed. The features we measured were:

- Volumes of each tissue type.
- The scleral canal opening diameter (Fig. 2). To measure the canal diameter, seventy-two landmarks (one every 5°) were placed on the reconstructed 3D model of the sclera at the opening of the scleral canal. A cross section of the reconstructed sclera, superimposed with the outlines of the scleral and laminar tissue, helped locate the landmark precisely. Landmark location could then be verified and adjusted in various 2D and 3D views of the model, including perspectives

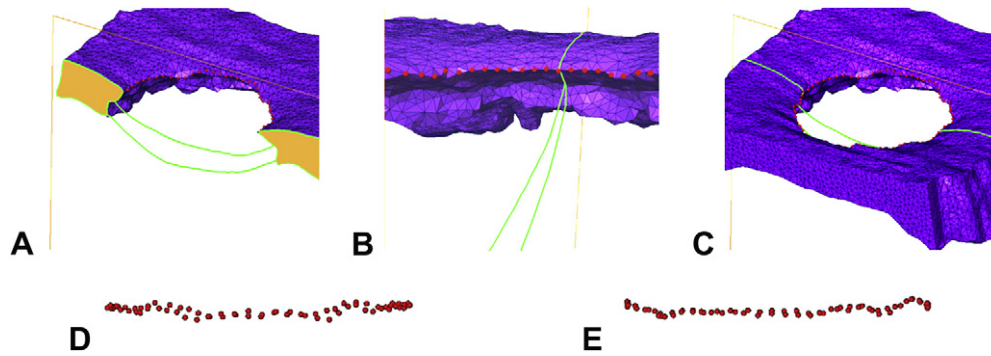


Fig. 2. Defining landmarks for measuring the diameter of the opening of the scleral canal. The reconstructed sclera is shown in purple, with the edges of the elements forming the surface shown in black; this enhances the apparent roughness on the surface and simplifies identifying the “tip” of the sclera that defines the margins of the scleral canal. For panel A only half the model is shown, with the interior of the sclera colored orange. The outlines of the sclera and LC are shown in green. In a view like that shown in Panel A the operator uses the mouse pointer (not shown) to define the location of a landmark, which is then marked by a red sphere. The location of a new landmark is restricted to a cut plane, visible in panels A, B and C by the orange outline. By sequentially rotating the cut plane in 5° increments the landmarks can be precisely located. The entire sclera with all landmarks defined is shown in Panel B. Once all landmarks have been placed, their locations can be verified by changing to a view from inside the canal (in perspective view, as opposed to all other views which are orthographic), as shown in Panel C. This view allows precise location of the landmarks in an anterior-posterior direction. As landmarks were defined, they could be displayed in side views to help identify outliers that may suggest section misalignment (Panels D and E, which are orthogonal views from the superior and nasal sides, respectively). (For interpretation of the references to colour in this figure legend, the reader is referred to the web version of this article.)

from inside the canal. The diameter of the scleral canal opening was then computed as the distance between opposite landmarks (i.e. those 180° apart). Superior-inferior and nasal-temporal scleral canal opening diameters were computed as the means in the desired direction $\pm 10^\circ$ to smooth out small variations. Scleral opening diameter eccentricity was computed as the ratio of the superior-inferior diameter to the nasal-temporal diameter.

- Area of the anterior and posterior LC surfaces, from which we computed the ratio of anterior to posterior LC surface area.
- The percentage of the anterior LC surface area visible through the scleral canal opening. This was determined by using the scleral canal opening as a mask to identify the region of the anterior LC surface not occluded (the region of the LC between the two vertical dashed lines in Fig. 3).
- The five following distances (key for Fig. 3 shown in parenthesis):
 1. The thickness of the LC, defined as the distance between the anterior (green line) and posterior (yellow line) surfaces of the LC.
 2. The thickness of the sclera, defined as the distance between the anterior (pink lines) and posterior (cyan lines) surfaces of the sclera. The scleral canal is defined by the red dots.
 3. The principal gradient length. This is the minimum distance between the anterior surface of the LC (green line) and the subarachnoid space (red lines). Given the high mechanical compliance of the pre-laminar neural tissue, some authors have assumed that the highest pressure gradient between IOP and CSF pressure occurs along this length and postulate that it could be an indicator of LC sensitivity to elevated IOP (Jonas et al., 2003; Morgan et al., 2002). We believe that the biomechanics of the ONH are more complex than this, but include this measure to allow comparison of the model reconstructions shown here with previous reports. We computed this distance using the anterior surface of the LC and the surfaces of the subarachnoid space, obtaining a population of distances. As a measure of the minimum principal gradient length we used the 5th percentile of the distribution, which reduced the influence of small irregularities in the surfaces due to artefacts of sectioning, staining or segmentation.
 4. and 5. The thickness of the pre-laminar neural tissue. This measure was subdivided into the thickness within

the cup and the thickness peripheral to the cup. The thickness within the cup was measured between the vitreo-retinal interface within the scleral canal (orange lines) and the anterior surface of the LC (green line). The thickness peripheral to the cup was measured between the vitreo-retinal interface exterior to the scleral canal (blue lines), and the anterior surface of the sclera (pink lines). It should be noted that our definition of cup is slightly different from the clinical one, which is usually defined as the region anterior to the vitreo-retinal interface and posterior to a certain reference plane (Burgoyne et al., 2005).

Although some of the measures listed above are not new in ONH morphometry, hence our calling them “traditional”, we emphasize that all measures were computed using the full 3D structure of the reconstructed ONH tissues. Fig. 3, which explains several of the measures, is simplified to a 2D representation. To compute the distance between surfaces we coded a custom software and computed the distance from all the nodes on the “source” surface to the nodes on the “target” surface using a “constrained minimum distance” method (Sigal, 2006). The method is similar to a minimum distance algorithm, but is more resistant to errors arising from noisy surfaces. Each of the triangular elements forming the source surface was assigned a distance to the target surface as the average of the distances for the nodes defining the element. When computing mean and percentile distances between surfaces the distances assigned to the elements were added and weighted by the element area to compensate for variations in element size over the surface.

Statistical analysis was carried out with the ANOVA data tools of Excel 2003 (Microsoft, Redmond Washington, USA). Statistical significance was defined as the probability of making a type one error of 5% ($p < 0.05$). The effects of IOP were indirectly assessed by comparing the measurements from contralateral eyes fixed at different IOPs. For the models reconstructed from the eyes of Donors 2 and 3 no comparison with a contralateral eye could be made since only one eye was reconstructed from each donor.

2.4. Lamina cribrosa insertion into the pia

While segmenting the region where the LC inserts into the sclera we were intrigued to observe that in many sections the LC

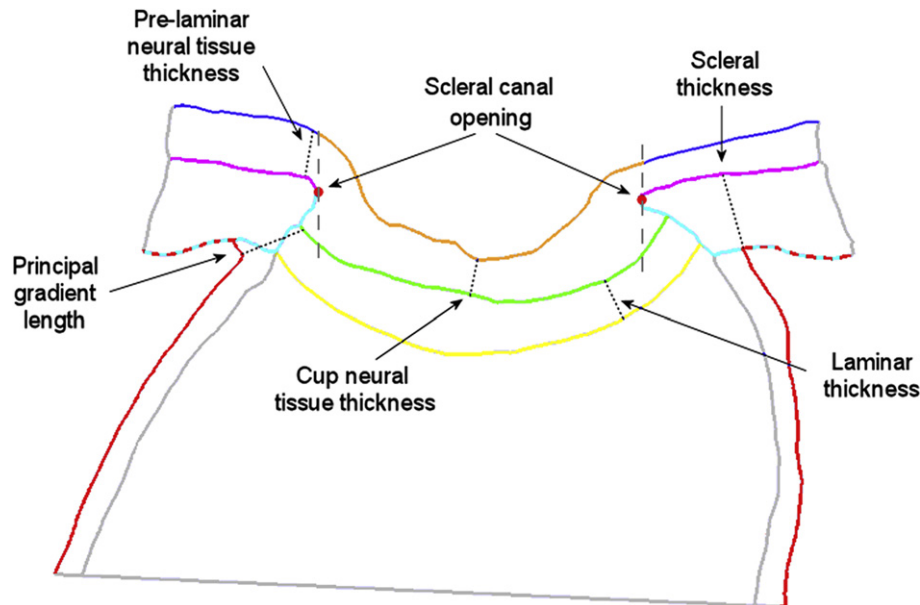


Fig. 3. Definitions of the thicknesses and distances measured from the specimen-specific models. The geometry is a sagittal section through the center of a specimen-specific model, with boundaries between tissue regions shown. Thicknesses and distances were computed between the highlighted surfaces (see text for details). Also defined were landmark points (red dots) to represent the scleral canal opening. Anterior-posterior lines through these landmark points (dashed lines) delimited the peripheral and cup regions of the pre-laminar neural tissue, as well as the region of the LC visible through the canal (see text for full description). (For interpretation of the references to colour in this figure legend, the reader is referred to the web version of this article.)

inserted, at least partially, into the pia mater. An example of this is shown in Fig. 4. Initially we considered if this may have been an artefact of the tissue processing or imaging in one section, but the feature was consistent in consecutive sections and across eyes. We therefore added to the analysis measures of the area of lamina inserting into the sclera and into the pia, and fraction of the LC insertion that is into the pia.

2.5. Quality control using a generic virtual eye

We validated the accuracy of our reconstruction and morphometry technique by applying it to a digital model of an idealized 3D eye (“a virtual eye”) in the same way as was done previously (Sigal et al., 2005b). Briefly, the virtual eye was generated by rotating the 2D Model 3 described in (Sigal et al., 2004) around its axis of symmetry, retaining the geometry and material properties of each tissue region. Virtual sections through the ONH of the virtual eye were generated, processed and analyzed in the same way as true histologic sections.

3. Results

Measurements taken on the original and reconstructed virtual eye ONH are compared in Table 2. Despite some small differences, the overall agreement was very good, with the errors averaging just over 1%. This is consistent with our previous evaluation of the technique (Sigal et al., 2005b), even though here we have compared several more measures than in the previous study, and helps to validate the reconstruction approach.

Summary information about ONH morphometry is listed in Table 3. The fraction of the LC which inserts into the pia averaged 12% (range 2–30%). The differences in measures between fellow eyes were generally smaller than the differences between unrelated eyes, despite of the large difference in IOP between fellow eyes, consistent with what has been observed in monkeys (Yang et al., *in press*). Mean scleral canal opening diameters ranged from 1346 to 1949 μm , and

although there was generally an increase in size with IOP it was not statistically significant ($p = 0.09$). The eccentricity of the scleral canal varied from 0.85 to 1.13 and was significantly larger in the higher IOP eyes ($p < 0.05$), with mean values of 0.974 and 1.098 at low and high IOP respectively. The ratio of anterior to posterior LC surface areas was smaller than one in all eyes, consistent with a curved LC. In paired eyes this ratio was always smaller in the low-pressure eye, but the differences were not statistically significant. The percentage of the LC visible through the scleral canal opening averaged 69% (range 58–83%; Table 3 and Fig. 5). This means that, on average, 31% of the anterior surface of the LC was hidden from view by the sclera. This value did not vary significantly with IOP.

Fig. 6 allows comparison between the morphometric data for the eyes of Donor 5 and results of a numerical simulation of the acute effects of IOP elevation. We have previously described the techniques for the numerical simulation (finite element modeling) of the acute biomechanical effects of changes in IOP (Sigal et al., 2005b, 2007a, 2009a,b). The simulations and morphometry share qualitative features (a wider LC and thinner cup neural tissue at elevated IOP). The models had predicted that the displacements of the LC due to IOP elevation were much larger in the lateral direction than in the anterior–posterior direction. The central region of the LC remained almost stationary as IOP increased, and the periphery stretched sideways due to lateral “pulling” on the LC by the sclera. The bottom of the cup also displaced minimally, with most of the predicted changes in cup shape being due to lateral displacement of the cup walls. However, simulations and morphometry do not agree well quantitatively. In an ideal situation, where contralateral eyes were identical and the histology, reconstruction and numerical modeling were perfect, then the middle and right columns of the bottom panel of Fig. 6 would be identical. At this point the origin of the differences is unclear, although it seems likely that the assumptions and approximations during the simulation are, at least, partially responsible.

It is of interest to compare the reconstructed LCs with a 3D version of the generic models used in some of the biomechanical

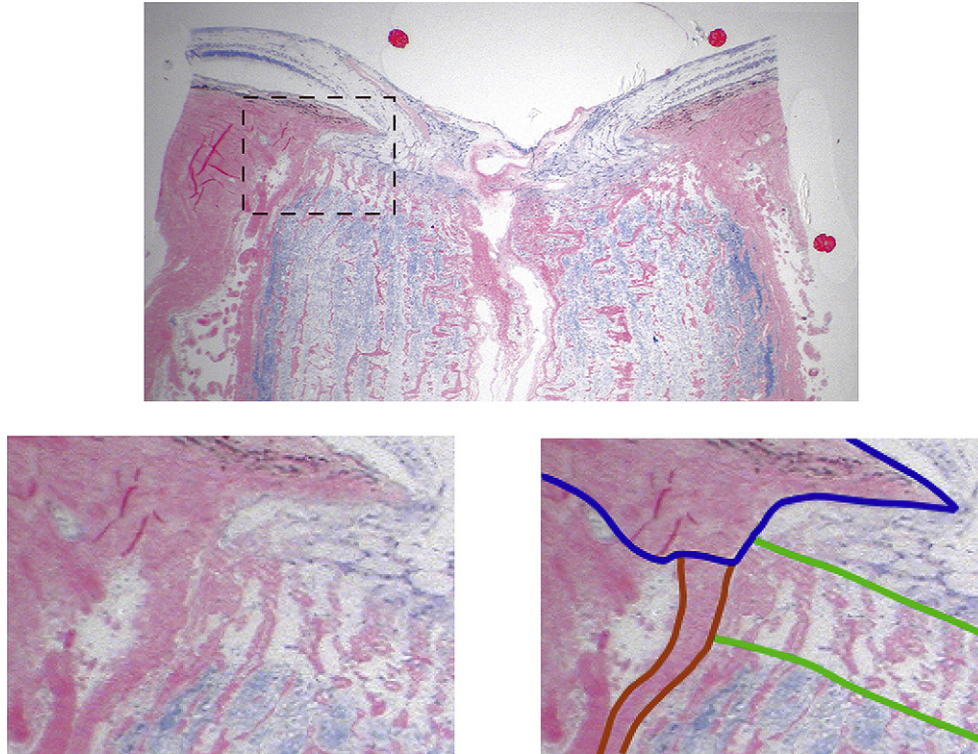


Fig. 4. Example of lamina cribrosa partially inserting into the pia mater. Shown is a superior-inferior section of the eye from Donor 2. The bottom left panel is a zoomed view of the rectangle marked in the top panel. The bottom right panel shows outlines of the regions segmented as lamina cribrosa (green), sclera (blue) and pia mater (red). The section is slightly temporal from the center of the scleral canal, which may explain the white ellipses on the pre-laminar neural tissue, likely RGC axonal bundles sectioned at an angle. Also clearly visible is the scleral “overhang” which occludes the LC from the front. Note that the segmentation was done in 3D following the process described in detail in the text, not from a single slide. (For interpretation of the references to colour in this figure legend, the reader is referred to the web version of this article.)

Table 2

Summary of morphometry on a virtual ONH to validate our techniques. See the text for details on how the different measures were defined and the data collected. Numbers were rounded to sufficient significant digits to show differences between true and reconstructed values.

Model	Generic Model		Error (%)
	Original	Reconstructed	
Area (mm ²)			
Posterior LC	3.7	3.72	0.63
Anterior LC	2.9	2.92	0.58
LC attachment to sclera	1.63	1.61	1.51
LC attachment to pia	0	0	–
Ratio of anterior to posterior LC areas	0.81	0.8	1.12
Area of anterior LC occluded by the sclera (%)	8	8.1	1.20
Scleral opening diameter (μm)			
Mean	1830	1818	0.63
SI	1830	1841	0.58
NT	1830	1839	0.52
Scleral opening eccentricity (SI/NT)	1.00	0.99	0.99
Mean thickness (μm)			
LC	260	259	0.34
Peripapillary sclera	514	524	2.01
Neural tissue Cup	405	409	1.08
Neural tissue Peripapillary	237	234	1.18
Minimum length (μm)			
Principal Gradient	143	146	1.97
Volume (μl)			
Total	30.2	29.98	0.74
ROI	8.8	8.73	0.83
Pre-laminar	2.1	2.12	1.12
Post-laminar	4.0	4.04	1.10
Sclera	1.5	1.47	1.70
Lamina	0.88	0.89	0.79
Pia	0.3	0.30	1.35
Average error over all measures			1.03

modeling (Sigal et al., 2004, 2005b) (Fig. 5, bottom panel). The geometry of the LC of the generic model was determined from the literature, before the specimen-specific models in this study were reconstructed. The comparison revealed good general agreement in LC size, shape and position in the canal.

4. Discussion and conclusions

This paper is the first to describe and apply a method for 3D morphometric analysis of ONH tissues to human eyes. To the best of our knowledge, this method is also the first to use an iterative approach for consistency and quality control, and where the segmentation of the ONH structures was carried out using multiple images concurrently (bright and dark-field in this case).

4.1. Results on human ONH morphometry

The main conclusions that arise from this work are that some eyes had a substantial amount of LC insertion into the pia mater, and not only into the sclera, and, on average 31% of the anterior LC surface area was “hidden” by the sclera. Let us consider these further:

In some eyes there was a substantial amount of LC inserting into the pia mater, and not only into the sclera. The percentage of LC inserting into the pia mater varied from 2.2 to 29.6% of the total insertion area. It also varied between contralateral eyes. To the best of our knowledge LC insertion into the pia mater has not been previously reported. Jonas and colleagues measured the length of “the posterior LC in direct contact with the pia mater and indirectly exposed to the cerebrospinal fluid space” (Jonas et al., 2003). They found in normal eyes a mean length of 39.4 μm, and a range of 0–334 μm. The biomechanical consequences of the LC inserting into the pia are still unclear, and likely depend on the mechanical

Table 3
Summary of morphometry on human ONHs. See the text for details on how the different measures were defined and the data collected. Only the scleral opening diameter eccentricity was significantly different between eyes at low and at high IOP ($p < 0.05$).

Donor	1	1	2	3	4	4	5	5	6	6
Eye	OD	OS	OD	OD	OD	OS	OD	OS	OD	OS
Fixation pressure [mmHg]	50	5	5	50	5	50	5	50	5	50
Area [mm ²]										
Posterior LC	3.7	3.6	3.6	4.6	4.0	3.3	4.8	4.7	4.4	4.4
Anterior LC	3.0	2.7	3.1	4.0	3.6	3.3	4.3	4.3	3.6	3.6
LC attachment to sclera	1.24	1.00	0.84	1.40	1.94	1.77	1.79	1.91	1.84	1.64
LC attachment to pia	0.07	0.03	0.17	0.26	0.34	0.04	0.22	0.14	0.40	0.69
Ratio of anterior to posterior LC areas	0.81	0.75	0.86	0.87	0.90	1.00	0.90	0.91	0.82	0.82
Area of anterior LC occluded by the sclera [%]	32	39	42	28	17	24	21	30	38	41
LC attachment on the pia [%]	5.3	2.9	16.8	15.7	14.9	2.2	10.9	6.8	17.9	29.6
Scleral opening diameter [μ m]										
Mean	1449	1346	1439	1735	1755	1707	1949	1837	1559	1516
SI	1497	1368	1252	1878	1747	1739	1940	1864	1621	1641
NT	1354	1365	1477	1567	1834	1698	1978	1828	1488	1453
Scleral opening eccentricity (SI/NT)	1.11	1.00	0.85	1.20	0.95	1.02	0.98	1.02	1.09	1.13
Mean thickness [μ m]										
LC	196	188	142	203	264	219	203	203	246	272
Peripapillary sclera	396	377	443	430	478	467	513	487	547	540
Neural tissue cup	558	656	428	337	422	393	402	350	471	494
Neural tissue peripapillary	313	346	247	234	318	306	328	257	324	316
Minimum length [μ m]										
Principal gradient	123	187	101	159	148	134	189	218	193	142
Volume [μ l]										
Total	13.2	15.9	15.2	18.6	22.2	21.5	24.5	26.0	22.9	19.1
ROI	10.9	11.4	11.9	13.2	12.6	15.4	14.6	15.0	14.6	14.3
Pre-laminar	2.6	2.7	2.2	2.8	2.5	3.4	2.5	3.2	3.1	2.3
Post-laminar	4.9	5.5	6.0	5.7	5.6	6.3	6.6	6.5	6.3	7.1
Sclera	1.5	1.5	1.8	2.0	1.8	3.0	2.6	2.6	2.6	2.4
Lamina	0.68	0.62	0.49	1.08	0.74	0.96	0.97	1.02	1.15	0.89
Pia	1.1	1.0	1.4	1.6	2.0	1.8	1.9	1.6	1.5	1.6

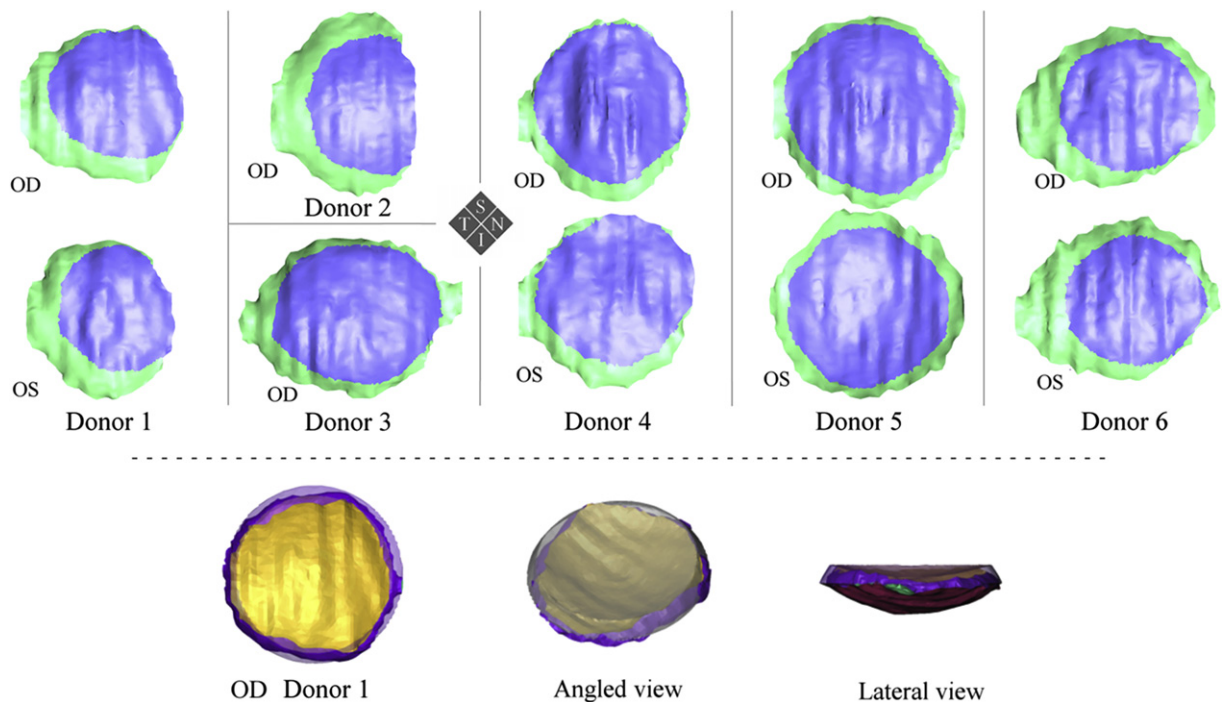


Fig. 5. Comparison of the LC of all reconstructed specimen-specific models and a generic model. Only one model was reconstructed from each of Donors 2 and 3. On the top panel are shown views from the front of the anterior LC surfaces with colors representing the region visible from the front (blue) or occluded by the sclera (green). In several eyes the center of the anterior LC surface was not aligned with the center of the scleral canal opening. On the bottom panel are shown three views from the OD model from Donor 1 superposed on a semi-transparent LC of a generic axisymmetric model (light purple). Colors represent the interface between the LC and the pre-laminar neural tissue (yellow) or the sclera (purple). The relative location of the specimen-specific and the generic LCs was determined through fitting the specimen-specific and generic peripapillary scleras. S-Superior, I-Inferior, N-Nasal, T-Temporal. (For interpretation of the references to colour in this figure legend, the reader is referred to the web version of this article.)

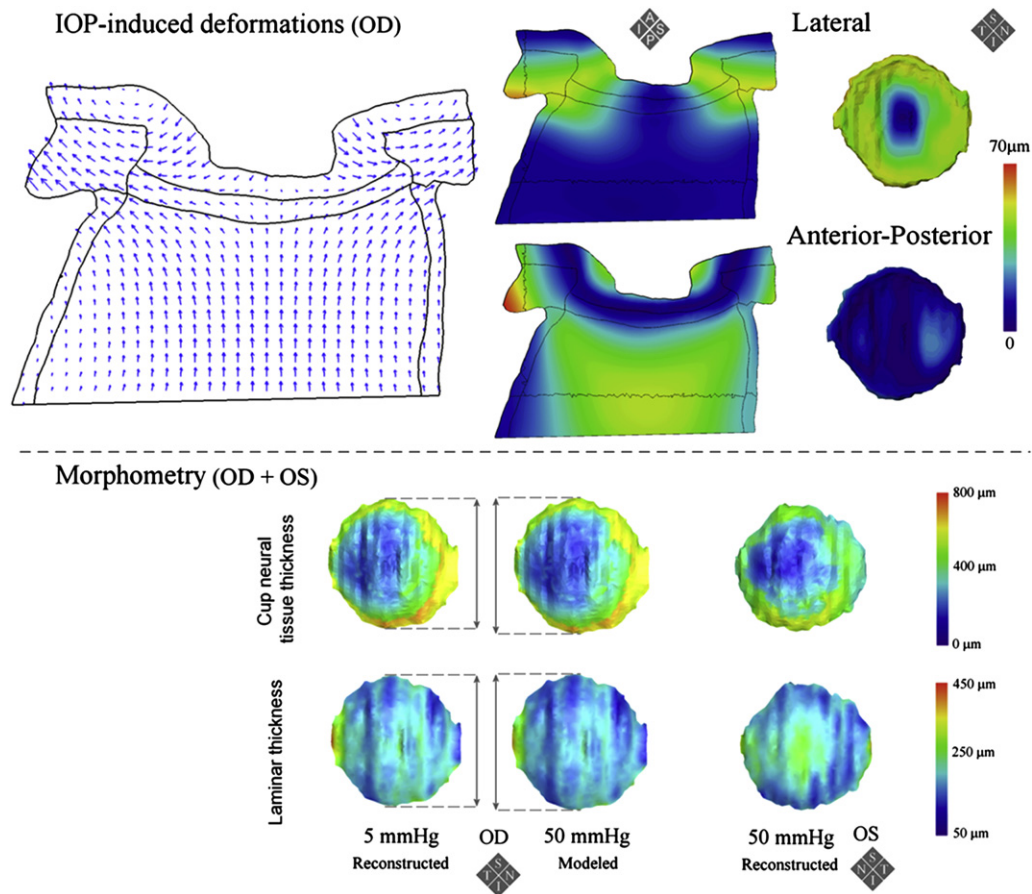


Fig. 6. Effects of an increase in IOP. Predicted IOP-induced deformations for the OD and OS of Donor 5. The top panel shows the results of a numerical simulation of an increase in IOP from 5 to 50 mmHg. On the left hand side are displacement vectors at the point of origin of the vector, overlaid on outlines of the ONH tissues. The vectors were computed in 3D, and it is their 2D projections that are shown. Vector lengths are proportional to the magnitude of the total displacement, with the scale exaggerated for clarity. The middle column in the top panel shows a two views of a sagittal cross section through the center of the model, whereas the rightmost column shows en-face (coronal) views of the LC. The models in the middle and right columns are colored according to the magnitude of predicted deformation in the lateral directions (top), or in the anterior-posterior direction (bottom). Predicted displacements are computed with respect to a reference ring on the vitreo-retinal interface 5° from the axis of symmetry. The bottom panel shows the results of morphometry. The geometries correspond to the two models reconstructed from the eyes of Donor 5 (left and right columns) and a the OD model simulated to an increase in IOP (middle column, the same model as in the top panel). Colors correspond to contour levels of the measures of lamina and cup neural tissue thickness. Arrows help compare the widths of the scleral canal opening and lamina cribrosa size at the different pressures. S-Superior, I-Inferior, N-Nasal, T-Temporal, A-Anterior, P-Posterior. (For interpretation of the references to colour in this figure legend, the reader is referred to the web version of this article.)

properties of the pia mater in this region. Although the LC insertion into the pia was clear in the histology, from the sections it is not possible to tell if the properties of the pia mater immediately adjacent to the LC are different from those of the pia mater elsewhere. In dogs the pia mater is thicker near the ONH (Balaratnasingam et al., 2009). The sections used for this study suggest that this is also true in human. In a separate study we used finite element modeling to investigate the influence of tissue material properties, including those of the pia, on ONH biomechanics (Sigal et al., 2009b). Although the stiffness of the pia mater was less influential than that of the sclera or LC, it was more influential in specimen-specific models with LC partially inserting into the pia, than in generic models where the LC attached only to the sclera.

On average, 31% of the anterior LC surface area was "hidden", or occluded, by the sclera. Between 17 and 42% of the anterior surface of the LC was occluded from view by the sclera (Table 3 and Fig. 5). This measure did not vary significantly with IOP. This large proportion could appear surprising when we look at an ONH cross section, such as that of the OD of Donor 5 in Fig. 6. Recall, however, that the ONH is a 3D structure, and areas that appear to be similar in magnitude in a cross section could actually represent very different ones in 3D. Further, our estimates of what could occlude the LC are conservative

since the LC could also be occluded by the Bruch's membrane, the vasculature and other tissues anterior to the LC (Downs et al., 2007; Yang et al., 2007a,b, in press). The area of occluded LC was asymmetric, with a larger proportion of the LC occluded on the temporal and inferior sides, representing an offset of the LC with respect to the scleral canal opening. The large fraction of occluded LC, and its asymmetry could be of clinical consequence if we consider that visual examination is still an important component of the analysis of the health of an optic disc in the clinic. They could also be of consequence for the development of newer methods of imaging the ONH, such as deep-scanning OCT (Agoumi et al., 2009; Inoue et al., 2009; Srinivasan et al., 2008; Strouthidis et al., 2008; Williams et al., 2009). Current OCT devices are incapable of penetrating the scleral tissue. If future devices still have this limitation, then it would be important to consider the proportion of LC that has been imaged when interpreting the data obtained using such devices. Simulations, such as those shown in Fig. 6, and discussed in more detail in (Sigal et al., 2007a, 2009a), predict that the majority of the IOP-induced deformation of the LC occur in the peripheral LC, and are therefore occluded from view by the sclera.

Other findings are also worth mentioning, although these have to be considered carefully in the light of the small sample size: scleral

canal eccentricity increased with IOP (all pairs); cup neural tissue (3 of 4 pairs) and pre-laminar neural tissue (all pairs) were thinner in the eye with the higher IOP; there was no difference in LC thickness between pairs of eyes at high and low IOPs; scleral canal diameters were more similar in contralateral eyes at different IOP than between unrelated eyes; the ratio of anterior to posterior LC surface was greatest in the high IOP eye (larger in 3 pairs, equal in one); and the variations in ONH morphology between eye pairs exceeded changes in morphology due to acute increases in IOP within an eye.

Changes in ONH morphometry produced by an increase in IOP were consistent with predictions made using numerical models with generic (Sigal et al., 2004, 2005b) or specimen-specific geometries (based on the same eyes in this study) (Sigal et al., 2007a, 2009a,b). For example the widening of the anterior surface of the LC shown in Fig. 6, and neural tissue thinning in the eye with the higher IOP. This confirms that the neural tissue anterior to the LC is deformable and that the vitreo-retinal interface is likely not a good surrogate for the LC deformations. The simulated increase in IOP from 5 to 50 mmHg produced an increase in mean scleral canal diameter of approximately 2.5%. This is very similar to the recent findings of Flanagan et al (Flanagan et al., 2009) who measured a 1.9% increase in normal, adult human eyes when IOP was increased over a similar range. Recent studies in monkey using 3D histomorphometry suggest that increases in IOP of 35 mmHg could produce scleral canal opening diameters between –3% (a contraction) and 10% (Yang et al., in press). It is likely that the majority of the increases in scleral canal diameter occur at low levels of IOP (Girard et al., 2009a,b; Woo et al., 1972).

In morphometry, scleral canal eccentricity increased with IOP (0.974 for low IOP and 1.098 for high IOP), whereas canal diameter did not. Eyes at high IOP had a more elongated scleral canal opening in the superior-inferior direction. The reason for this is still unclear, although simulations with models of the ONH embedded in scleral shells with realistic scleral thickness distributions predict differential stresses and strains around the ONH that could lead to changes in canal eccentricity with IOP (Roberts et al., 2007; Sigal et al., 2007b). Analytical models of the ONH have suggested that scleral canal eccentricity could be an important determinant of IOP-induced strain within the LC (Sander et al., 2006).

There are only a few morphometric studies of the human ONH that report measures that can be directly compared with the ones in this work. Perhaps the most comprehensive ones are those of Jonas et al. (Jonas et al., 2003, 2004, 1991; Jonas and Hayreh, 1999; Jonas and Holbach, 2005). Our measures are closer to the values Jonas reported for eyes with glaucoma than for normal eyes. For example, while we measured a mean lamina thickness of 245 μm , they report 458 μm in normal eyes and 201 μm in glaucomatous eyes. Although this could suggest that the eyes on which we based the models used in this study were glaucomatous, this is not necessarily the case. The mean lamina thicknesses of our models are between 146 and 278 μm , falling within the range of measures reported by Jonas for normal eyes: 92–1008 μm ; and also within the range for glaucomatous eyes: 30–868 μm . A similar situation occurs for the principal gradient length, and the ratios of the areas of anterior to posterior LC surfaces which can be compared with Jonas' report (Jonas et al., 2003). Our measurements of lamina thickness are also lower than the 345.6–555.9 μm reported by Kotecha and colleagues (Kotecha et al., 2006), even though the eyes in our study are within the older range in their study. Besides natural differences between specimens, it is possible that a reason why our measurements were on the lower end of other reports is that our measurements were performed in 3D, and each study used different histological techniques. Like ours, previous studies also found large overlaps in the morphometry values between conditions, such as normal and glaucoma (Downs

et al., 2007; Jonas et al., 2003; Jonas and Holbach, 2005; Yang et al., 2007a), normal and high myopes (Jonas et al., 2004), or low and elevated IOP (Bellezza et al., 2003; Yang et al., in press). Recent studies have found that physiologic differences between contralateral eyes are relatively small compared with inter-individual differences (Yang et al., in press).

4.2. Evaluating the methodology

We evaluated the morphometry technique by using it on a virtual eye of known dimensions. The differences between the dimensions measured through our method and the actual dimensions were small, which is encouraging, and strongly suggests that the reconstruction and morphometry techniques we present provide good measures of the ONH shape. However, we should note that there are some substantial differences between virtual and real tissue sections: virtual sections are perfectly aligned, suffer no deformation or shrinkage, and all tissue boundaries are unequivocal. We should, therefore, think of the reconstruction of the generic virtual eye as a “best-case” scenario. For an extended discussion of the evaluation of the method, including reconstructions of the ONH vasculature, and simulation predictions between original and reconstructed models see (Sigal et al., 2005b).

Our methodology is related to, but was developed independently of, techniques for the morphometric analysis of the monkey ONH (Downs et al., 2007; Yang et al., 2007a,b, in press). Both techniques, therefore, share many of the benefits, such as the ability to derive 3D measures, and limitations, including inhomogeneous staining and ambiguity in the definition of the landmarks and structures. However, there are some notable differences. Most important, the use of block (as opposed to cut section) imaging used in (Downs et al., 2007; Yang et al., 2007a,b, in press) reduces problems related to section deformation and thus requires no unwarping and permits the collection of more images at higher resolution.

4.2.1. Improvements of our technique compared with traditional methods

Iterative checking: Adopting an iterative process, in which the geometric quality of a model is evaluated and the model is refined until a series of requirements is satisfied, helped improve the measurements carried out on the models by ensuring that all features of the model (and hence measurements based on them) were consistent with one another. Traditional 2D histomorphometric analysis of isolated sections has little opportunity to compensate for deformations or other problems that could have occurred during section preparation, even with experienced operators. (See (Sigal et al., 2005b) for a discussion of possible geometric artefacts that can be introduced in sample preparation).

4.2.1.1. Measurement in 3D. Problems with carrying out measurements on single sections in histologic analysis have been previously discussed (Jonas et al., 2003; Jonas and Holbach, 2005; Yan et al., 1994). One issue is that measurements taken from such sections are potentially susceptible to bias. Measurement of the thickness of the LC is a good example of this: given the curved shape of the lamina, and that it is offset and not centered on the scleral canal opening, sections taken through the center of the canal may be lateral on the LC, and at an angle. Measurements on these sections may overestimate the thickness of the LC or not represent the correct locations. Another example is the minimal gradient length introduced by Jonas et al (Jonas et al., 2003). This minimum distance between two complex 3D surfaces, those of the anterior surface of the LC and of the subarachnoid space, is more reliably determined in 3D.

4.2.1.2. More clearly defined landmarks. Definition and identification of landmarks for morphometric analysis is more reliable when done in 3D views, where several orientations are visible simultaneously. See below for additional discussion of landmark definition.

4.2.1.3. Flexibility in source of images. ONH components were not all best identified under the same staining and imaging conditions. Specifically, some components were clearer in dark-field imaging, while others required stained bright field images. As presented here, the method for reconstructing ONH models used two types of ONH images, but the method could be extended to include more types, including non-histological sections. Combining the various imaging techniques into one consistent model potentially allows improving the quality of the measurements, as well as an evaluation of the imaging procedures themselves.

4.2.1.4. Method also provides models for FEM. Our method also produces models suitable for finite element analysis. Although this work is not the first one to present results of specimen-specific models of the ONH (Sigal et al., 2007a, 2009a,b), we have presented here some results of modeling because we believe these are useful in the analysis of the morphometry data which is the focus of this work.

4.2.2. Limitations

Our method also has some limitations. Limitations related to the use of serial histological sections have been discussed in (Sigal et al., 2005b), and included use of ex vivo tissue and geometric artefacts introduced during preparation and reconstruction. Other limitations of the reconstruction method were the non-trivial definition of the landmarks (including some tissue boundaries) and the ambiguity in the definition of some measures. These last two limitations merit some additional discussion. Definition of landmarks in an accurate and repeatable way is not trivial. For some structures, like the posterior surface of the LC, the definition can be particularly difficult. This problem occurs to some degree in all morphometric analyses, and could be responsible for some of the differences observed between our measures and those in previous reports. In 3D the definition of quantities like thickness or distance between two surfaces is not unambiguous. Depending on the context there are many ways in which these quantities can be defined. We believe that using definitions that consider the 3D nature of the ONH is more likely to lead to useful measures.

This work relies on the use of post mortem eyes, and we cannot exclude the possibility that degenerative changes after death could have altered some aspects of ONH anatomy. This is an intrinsic limitation of all histology-based studies. Another possible confounding factor is the absence of circulation post mortem. Depending on the extent of thrombus formation, vessels may have changed volume due to blood being expelled under high fixation pressure, and this could subtly change some aspects of the measured anatomic features. It should also be noted that our model of acute IOP elevation does not mimic the long-term remodeling changes that would occur in vivo in an eye chronically exposed to elevated IOP.

Finally, the main problem with the morphometric analysis presented herein is that it is more time-consuming than 2D histologic analysis. The initial models shown in (Sigal et al., 2005b) required approximately three months from initial section preparation to FE modeling. Through practice and algorithm streamlining this time has been reduced to about one week per model, but this is still considerably more time than is required for traditional histologic analysis and was the main factor limiting the number of specimen-specific models considered in this study.

5. Conclusion

We have shown what we believe are the first 3D morphometric analyses of the human ONH. On average, about one third of the anterior LC surface was obscured from view by the sclera. In all eyes the LC inserted into the pia mater and not only into the sclera. There were some trends observed in measurements carried out in contralateral eyes fixed at different pressures, like the increase in scleral canal eccentricity and the thinning of pre-laminar structures with increasing IOP. The changes were often consistent with what was predicted using finite element simulations in (Sigal et al., 2005a, 2004, 2009a), yet simulating a change in IOP did not “remove” the differences in geometry between contralateral eyes fixed at different IOP. Future work could benefit from an increase in the sample size. We believe that these results are valuable for the study of ONH anatomy in general, and can potentially contribute to the analysis of ONH biomechanics.

Acknowledgements

We thank the Eye Bank of Canada for providing donor tissue, and Ashwin Wagadarikar for his contributions to coding the custom Amira modules.

References

- Agoumi, Y., Artes, P.H., Nicolela, M.T., Chauhan, B.C., 2009. Spectral Domain Optical Coherence Tomography Measurements of Lamellar and Prelaminar Tissue Movement After Intraocular Pressure Elevation. ARVO Meeting of the Association for Research in Vision and Ophthalmology, Ft. Lauderdale 2009.
- Albon, J., Farrant, S., Akhtar, S., Young, R., Boulton, M.E., Smith, G., Taylor, M., Guggenheim, J., Morgan, J.E., 2007. Connective tissue structure of the optic nerve head and associated ageing changes. *Invest. Ophthalmol. Vis. Sci.* 48 (5), 2134–2144.
- Balaratnasingam, C., Morgan, W.H., Johnstone, V., Pandav, S.S., Cringle, S.J., Yu, D.Y., 2009. Histomorphometric measurements in human and dog optic nerve and an estimation of optic nerve pressure gradients in human. *Exp. Eye Res.*
- Bellezza, A.J., Rintalan, C.J., Thompson, H.W., Downs, J.C., Hart, R.T., Burgoyne, C.F., 2003. Anterior scleral canal geometry in pressurised (IOP 10) and non-pressurised (IOP 0) normal monkey eyes. *Br. J. Ophthalmol.* 87 (10), 1284–1290.
- Burgoyne, C.F., Downs, J.C., Bellezza, A.J., Suh, J.K., Hart, R.T., 2005. The optic nerve head as a biomechanical structure: a new paradigm for understanding the role of IOP-related stress and strain in the pathophysiology of glaucomatous optic nerve head damage. *Prog. Retin. Eye Res.* 24 (1), 39–73.
- Burgoyne, C.F., Morrison, J.C., 2001. The anatomy and pathophysiology of the optic nerve head in glaucoma. *J. Glaucoma* 10 (5 Suppl.1), S16–S18.
- Burgoyne, C.F., Varma, R., Quigley, H.A., Vitale, S., Pease, M.E., Lenane, P.L., 1994. Global and regional detection of induced optic disc change by digitized image analysis. *Arch. Ophthalmol.* 112 (2), 261–268.
- Downs, J.C., Yang, H., Girkin, C., Sakata, L., Bellezza, A., Thompson, H., Burgoyne, C.F., 2007. Three-dimensional histomorphometry of the normal and early glaucomatous monkey optic nerve head: neural canal and subarachnoid space architecture. *Invest. Ophthalmol. Vis. Sci.* 48 (7), 3195–3208.
- Flanagan, J.G., Costanz, C., Tertinegg, I., Wong, T., Trope, G.E. 2009. Choroidal Thickness Changes in Response to Acute Increase in Intraocular Pressure. ARVO Meeting of the Association for Research in Vision and Ophthalmology, Ft. Lauderdale 2009.
- Girard, M.J., Downs, J.C., Burgoyne, C.F., Suh, J.K., 2009a. Peripapillary and posterior scleral mechanics—part I: development of an anisotropic hyperelastic constitutive model. *J. Biomech. Eng.* 131 (5), 051011.
- Girard, M., Downs, J., Bottlang, M., Burgoyne, C.F., Suh, J.K., 2009b. Peripapillary and posterior scleral mechanics—part II: experimental and inverse finite element characterization. *J. Biomech. Eng.* 131 (5), 051012.
- Hecksher-Sorensen, J., Sharpe, J., 2001. 3D confocal reconstruction of gene expression in mouse. *Mech. Dev.* 100 (1), 59–63.
- Hernandez, M.R., 2000. The optic nerve head in glaucoma: role of astrocytes in tissue remodeling. *Prog. Retin. Eye Res.* 19 (3), 297–321.
- Inoue, R., Hangai, M., Kotera, Y., Nakanishi, H., Mori, S., Morishita, S., Yoshimura, N., 2009. Three-dimensional high-speed optical coherence tomography imaging of lamina cribrosa in glaucoma. *Ophthalmology* 116 (2), 214–222.
- Jonas, J.B., Berenshtein, E., Holbach, L., 2003. Anatomic relationship between lamina cribrosa, intraocular space, and cerebrospinal fluid space. *Invest. Ophthalmol. Vis. Sci.* 44 (12), 5189–5195.
- Jonas, J.B., Berenshtein, E., Holbach, L., 2004. Lamina cribrosa thickness and spatial relationships between intraocular space and cerebrospinal fluid space in highly myopic eyes. *Invest. Ophthalmol. Vis. Sci.* 45 (8), 2660–2665.
- Jonas, J.B., Budde, W.M., 2000. Diagnosis and pathogenesis of glaucomatous optic neuropathy: morphological aspects. *Prog. Retin. Eye Res.* 19 (1), 1–40.

- Jonas, J.B., Hayreh, S.S., 1999. Optic disk morphology in experimental central retinal artery occlusion in rhesus monkeys. *Am. J. Ophthalmol.* 127 (5), 523–530.
- Jonas, J.B., Holbach, L., 2005. Central corneal thickness and thickness of the lamina cribrosa in human eyes. *Invest. Ophthalmol. Vis. Sci.* 46 (4), 1275–1279.
- Jonas, J.B., Mardin, C.Y., Schlotzer-Schrehardt, U., Naumann, G.O., 1991. Morphometry of the human lamina cribrosa surface. *Invest. Ophthalmol. Vis. Sci.* 32 (2), 401–405.
- Kotecha, A., Izadi, S., Jeffery, G., 2006. Age-related changes in the thickness of the human lamina cribrosa. *Br. J. Ophthalmol.* 90 (12), 1531–1534.
- Morgan, W.H., 1999. *Pressure Gradients Across the Optic Disk* [Doctoral]. The University of Western Australia, pp. 271.
- Morgan, W.H., Chauhan, B.C., Yu, D.Y., Cringle, S.J., Alder, V.A., House, P.H., 2002. Optic disc movement with variations in intraocular and cerebrospinal fluid pressure. *Invest. Ophthalmol. Vis. Sci.* 43 (10), 3236–3242.
- Oyama, T., Abe, H., Ushiki, T., 2006. The connective tissue and glial framework in the optic nerve head of the normal human eye: light and scanning electron microscopic studies. *Arch. Histol. Cytol.* 69 (5), 341–356.
- Quigley, H.A., Addicks, E.M., 1981. Regional differences in the structure of the lamina cribrosa and their relation to glaucomatous optic nerve damage. *Arch. Ophthalmol.* 99 (1), 137–143.
- Quigley, H.A., Addicks, E.M., Green, W.R., Maumenee, A.E., 1981. Optic nerve damage in human glaucoma. II. The site of injury and susceptibility to damage. *Arch. Ophthalmol.* 99 (4), 635–649.
- Roberts, M.D., Hart, R.T., Liang, Y., Bellezza, A., Burgoyne, C.F., Downs, J., 2007. Continuum-level finite element modeling of the optic nerve head using a fabric tensor based description of the lamina cribrosa; Keystone, Colorado.
- Sander, E.A., Downs, J.C., Hart, R.T., Burgoyne, C.F., Nauman, E.A., 2006. In-plane mechanics of the optic nerve head with cellular solids models. Munich, Germany. *J. Biomech.*, S385. July 29–August 4.
- Sigal, I.A., 2006. *Human Optic Nerve Head Biomechanics: an Analysis of Generic and Individual-specific Models Using the Finite Element Method* [Doctoral]. University of Toronto, Toronto.
- Sigal, I.A., 2009. Interactions between geometry and mechanical properties on the optic nerve head. *Invest. Ophthalmol. Vis. Sci.* 50 (6), 2785–2795.
- Sigal, I.A., Flanagan, J.G., Ethier, C.R., 2005a. Factors influencing optic nerve head biomechanics. *Invest. Ophthalmol. Vis. Sci.* 46 (11), 4189–4199.
- Sigal, I.A., Flanagan, J.G., Tertinegg, I., Ethier, C.R., 2004. Finite element modeling of optic nerve head biomechanics. *Invest. Ophthalmol. Vis. Sci.* 45 (12), 4378–4387.
- Sigal, I.A., Flanagan, J.G., Tertinegg, I., Ethier, C.R., 2005b. Reconstruction of human optic nerve heads for finite element modeling. *Technol. Health Care* 13 (4), 313–329.
- Sigal, I.A., Flanagan, J.G., Tertinegg, I., Ethier, C.R., 2007a. Predicted extension, compression and shearing of optic nerve head tissues. *Exp. Eye Res.* 85 (3), 312–322.
- Sigal, I.A., Flanagan, J.G., Tertinegg, I., Ethier, C.R., 2009a. Modeling individual-specific human optic nerve head biomechanics. Part I: IOP-induced deformations and influence of geometry. *Biomech. Model. Mechanobiol.* 8 (2), 85–98.
- Sigal, I.A., Flanagan, J.G., Tertinegg, I., Ethier, C.R., 2009b. Modeling individual-specific human optic nerve head biomechanics. Part II: influence of material properties. *Biomech. Model. Mechanobiol.* 8 (2), 99–109.
- Sigal, I.A., Norman, R.E., Rausch, S.M.K., Tertinegg, I., Eilaghi, A., Morgan, K., Portnoy, S., Sled, J.G., Flanagan, J.G., Ethier, C.R., 2007b. Mechanics of individual-specific models of the corneo-scleral shell in glaucoma. E-abstract 3306. *Invest. Ophthalmol. Vis. Sci.* 48.
- Srinivasan, V.J., Adler, D.C., Chen, Y., Gorczynska, I., Huber, R., Duker, J.S., Schuman, J.S., Fujimoto, J.G., 2008. Ultrahigh-speed optical coherence tomography for three-dimensional and en face imaging of the retina and optic nerve head. *Invest. Ophthalmol. Vis. Sci.* 49 (11), 5103–5110.
- Strouthidis, N.G., Yang, H., Fortune, B., Downs, J.C., Burgoyne, C.F., 2008. Detection of the optic nerve head neural canal opening within three-dimensional histomorphometric and Spectral Domain optical coherence tomography data Sets. *Invest. Ophthalmol. Vis. Sci.*
- Wells, A.P., Garway-Heath, D.F., Poostchi, A., Wong, T., Chan, K.C., Sachdev, N., 2008. Corneal hysteresis but not corneal thickness correlates with optic nerve surface compliance in glaucoma patients. *Invest. Ophthalmol. Vis. Sci.* 49 (8), 3262–3268.
- Williams, G., Strouthidis, N.G., Fortune, B., Yang, H., Grimm, J., Reynaud, J., Cull, G., Wang, L., Burgoyne, C.F., 2009. Detection of Longitudinal Optic Nerve Head (ONH) and Retinal Nerve Fiber Layer Thickness (RNFLT) Changes In Experimental Glaucoma Using Spectral Domain Optical Coherence Tomography (SD-OCT). ARVO Meeting of the Association for Research in Vision and Ophthalmology, Ft. Lauderdale 2009.
- Woo, S.L., Kobayashi, A.S., Schlegel, W.A., Lawrence, C., 1972. Nonlinear material properties of intact cornea and sclera. *Exp. Eye Res.* 14 (1), 29–39.
- Yan, D.B., Coloma, F.M., Metheerairat, A., Trope, G.E., Heathcote, J.G., Ethier, C.R., 1994. Deformation of the lamina cribrosa by elevated intraocular pressure. *Br. J. Ophthalmol.* 78 (8), 643–648.
- Yan, D.B., Flanagan, J.G., Farra, T., Trope, G.E., Ethier, C.R., 1998. Study of regional deformation of the optic nerve head using scanning laser tomography. *Curr. Eye Res.* 17 (9), 903–916.
- Yang, H., Downs, J.C., Bellezza, A.J., Thompson, H., Burgoyne, C.F., 2007a. 3-D histomorphometry of the normal and early glaucomatous monkey optic nerve head: prelaminar neural tissues and Cupping. *Invest. Ophthalmol. Vis. Sci.* 48 (11), 5068–5084.
- Yang, H., Downs, J.C., Burgoyne, C.F., 2009. Physiologic intereye differences in monkey optic nerve head architecture and their relation to changes in early experimental glaucoma. *Invest. Ophthalmol. Vis. Sci.* 50 (1), 224–234.
- Yang, H., Downs, J.C., Girkin, C., Sakata, L., Bellezza, A., Thompson, H., Burgoyne, C.F., 2007b. 3-D histomorphometry of the normal and early glaucomatous monkey optic nerve head: lamina cribrosa and peripapillary scleral position and thickness. *Invest. Ophthalmol. Vis. Sci.* 48 (10), 4597–4607.
- Yang, H., Downs, J.C., Sigal, I.A., Roberts, M.D., Thompson, H., Burgoyne, C.F. Deformation of the Normal Monkey Optic Nerve Head Connective Tissue Following under Acute IOP Elevation. *Invest. Ophthalmol. Vis. Sci.*, in press. doi:10.1167/iov.09-3410.